



Cite as  
Nano-Micro Lett.  
(2024) 16:234

Received: 7 March 2024  
Accepted: 30 April 2024  
© The Author(s) 2024

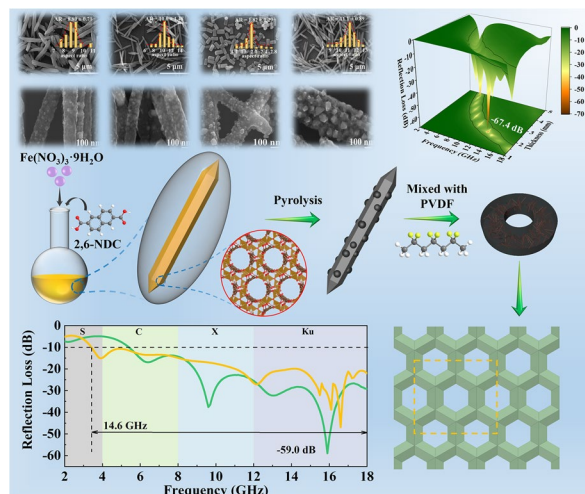
# Designing Symmetric Gradient Honeycomb Structures with Carbon-Coated Iron-Based Composites for High-Efficiency Microwave Absorption

Yu Zhang<sup>1</sup>, Shu-Hao Yang<sup>1</sup>, Yue Xin<sup>1</sup>, Bo Cai<sup>1</sup>, Peng-Fei Hu<sup>1</sup>, Hai-Yang Dai<sup>2</sup>, Chen-Ming Liang<sup>3</sup>, Yun-Tong Meng<sup>3</sup>, Ji-Hao Su<sup>3</sup>, Xiao-Juan Zhang<sup>4</sup>✉, Min Lu<sup>3</sup>✉, Guang-Sheng Wang<sup>1</sup>✉

## HIGHLIGHTS

- MIL-88C (Fe) with varying aspect ratios as a precursor was synthesized by regulating oil bath conditions, followed by one-step thermal decomposition to obtain carbon-coated iron-based composites.
- High-efficiency microwave absorption properties were achieved with  $RL_{\min}$  value of -67.4 dB (2.13 mm) and wide effective absorption bandwidth (EAB) of 5.52 GHz (1.90 mm) under the low filler loading.
- A symmetric gradient honeycomb structure was constructed utilizing the high-frequency structure simulator, achieving an EAB of 14.6 GHz and a  $RL_{\min}$  of -59.0 dB.

**ABSTRACT** The impedance matching of absorbers is a vital factor affecting their microwave absorption (MA) properties. In this work, we controllably synthesized Material of Institute Lavoisier 88C (MIL-88C) with varying aspect ratios (AR) as a precursor by regulating oil bath conditions, followed by one-step thermal decomposition to obtain carbon-coated iron-based composites. Modifying the precursor MIL-88C (Fe) preparation conditions, such as the molar ratio between metal ions and organic ligands (M/O), oil bath temperature, and oil bath time, influenced the phases, graphitization degree, and AR of the derivatives, enabling low filler loading, achieving well-matched impedance, and ensuring outstanding MA properties. The MOF-derivatives 2 (MD<sub>2</sub>)/polyvinylidene Difluoride (PVDF), MD<sub>3</sub>/PVDF, and MD<sub>4</sub>/PVDF absorbers all exhibited excellent MA properties with optimal filler loadings below 20 wt% and as low as 5 wt%. The MD<sub>2</sub>/PVDF (5 wt%) achieved a maximum effective absorption bandwidth (EAB) of 5.52 GHz (1.90 mm). The MD<sub>3</sub>/PVDF (10 wt%) possessed a minimum reflection loss ( $RL_{\min}$ ) value of -67.4 at 12.56 GHz (2.13 mm). A symmetric gradient honeycomb structure (SGHS) was constructed utilizing the high-frequency structure simulator (HFSS) to further extend the EAB, achieving an EAB of 14.6 GHz and a  $RL_{\min}$  of -59.0 dB. This research offers a viable inspiration to creating structures or materials with high-efficiency MA properties.



**KEYWORDS** MIL-88C (Fe); Fe/Fe<sub>3</sub>O<sub>4</sub>/Fe<sub>3</sub>C@C; Controllable preparation; Symmetric gradient honeycomb structure; Microwave absorbing

✉ Xiao-Juan Zhang, zhxiaojuan@btbu.edu.cn; Min Lu, 19770919@163.com; Guang-Sheng Wang, wanggsh@buaa.edu.cn

<sup>1</sup> School of Chemistry, Beihang University, Beijing 100191, People's Republic of China

<sup>2</sup> School of Electronics and Information, Zhengzhou University of Light Industry, Zhengzhou 450002, People's Republic of China

<sup>3</sup> School of Chemical Engineering, Northeast Electric Power University, Jilin 132000, People's Republic of China

<sup>4</sup> College of Chemistry and Materials Engineering, Beijing Technology and Business University, Beijing 100048, People's Republic of China



## 1 Introduction

In the contemporary era, electromagnetic (EM) technology is undergoing continuous development and finds widespread applications in both military and civilian domains, including military radar, portable electronics, wireless communication, and more [1–3]. While EM technology provides substantial convenience, it also gives rise to electromagnetic interference and radiation, posing risks to people's wellness [4–6], and impacting the regular operation of electronic devices. To address the aforementioned challenges, the development of materials that can absorb electromagnetic waves, particularly microwaves, is an imperative. Microwave absorbing materials (MAM) can be categorized into three groups based on distinct absorption mechanisms: materials with dielectric loss, magnetic loss, and composite loss [7]. Dielectric loss materials primarily encompass carbon-based materials [8–10], MXene [11], non-magnetic metal compounds [12], and nonmetallic compounds [13]. Notably, carbon-based materials have garnered significant attention owing to their distinctive properties, including lightweight characteristics, suitability for practical engineering applications, and favorable electrical properties. Magnetic loss materials predominantly consist of magnetic metals [14] and their compounds [15]. Adequate impedance matching is a fundamental requirement for optimal microwave absorbing material (MAM) performance. Individual dielectric loss materials or magnetic loss materials alone cannot achieve effective impedance matching. Combining both types can overcome the aforementioned limitations [16].

Metal–organic frameworks (MOF) are coordination polymers comprising metal ions coordinated with organic ligands, forming intricate structures with diverse functionalities and applications. Composites comprising magnetic metals or their compounds coated with carbon can be synthesized by controlling pyrolysis conditions. These composites effectively combine dielectric losses from carbon materials and magnetic losses from either magnetic metals or their compounds, thereby enhancing impedance matching and MA performance [17]. Currently, several studies on iron-based MOF derivatives with abundant metal element reserves and low costs have been conducted. Among the iron-based MOF, the MIL-88 series comprises four subtypes: 88A (fumaric acid), 88B (terephthalic acid, 1,4-BDC), 88C (2,6-naphthalenedicarboxylic, 2,6-NDC), and

88D (4,4'-biphenyldicarboxylic, 4-4'-BPDC), distinguished by different organic ligands [18, 19]. Among them, MIL-88C is characterized by a short synthesis cycle and a large AR. According to percolation theory, the larger the AR of one-dimensional (1D) materials, the lower the percolation threshold value. This scenario is conducive to achieving optimal MA performance at low filler levels [20]. Previous studies have demonstrated that different ligands can influence the EM parameters of the corresponding derivatives, thereby impacting MA performance [21]. Wu et al. [22] utilized MIL-88A as a precursor to synthesize the absorber  $\text{Fe}_3\text{O}_4/\text{Fe}_3\text{C}@C$  through pyrolysis at 600 °C. The  $RL_{\min}$  was -52.9 dB at 11.68 GHz (3.07 mm) and a higher filler loading of 40 wt%, achieving a EAB of 4.56 GHz at 3.5 mm. Xiong et al. [23] synthesized  $\text{Fe}_3\text{O}_4@$ nanoporous carbon (NPC) composites by calcining Fe-MIL-88B. With a high filling amount of 30 wt%,  $\text{Fe}_3\text{O}_4@NPC$  exhibited a  $RL_{\min}$  of -65.5 dB at 9.8 GHz, while exhibiting an undesirable EAB of 4.5 GHz (3 mm). All of the aforementioned absorbers exhibited high filler amounts, narrow EAB, and thick matching thicknesses. Additionally, current research has focused on investigating the impact of pyrolysis conditions on MA properties. The influence of varying preparation conditions of the precursors on the MA properties of derivatives has been scarcely investigated.

The potential for practical engineering applications of single MAM is somewhat limited by inherent constraints. Numerous materials with unique structures exhibit MA properties surpassing those of natural materials, especially EAB [24–26]. The honeycomb structure has gained prominence in current research due to its lightweight and high-strength characteristics [27, 28]. Impedance matching and attenuation capabilities are pivotal considerations in determining MA properties. Conventional through-hole honeycomb structures possess certain MA properties but do not independently isolate the two aforementioned factors. The entire honeycomb through-hole is responsible for both the entry and absorption of microwaves. Designing a structure that optimizes these two factors separately can more effectively leverage structural advantages and exhibit enhanced MA properties.

Herein, we controllably synthesized MIL-88C (Fe) as a precursor with varying AR using an oil bath under diverse conditions, followed by one-step thermal decomposition to obtain the corresponding carbon-coated iron-based composites. The influence of MIL-88C (Fe) preparation conditions

on the MA properties of the derivatives was investigated, including M/O, oil bath temperature, and oil bath time. Consequently, the phases, graphitization degree, and AR of the derivatives were influenced to attain low filler loading, optimize impedance matching, and enhance MA performance. As anticipated, the composites derived from MIL-88C (Fe) fabricated under a diverse range of conditions consistently displayed outstanding MA properties, including low loading, strong absorption, broad EAB, and thin thickness. We also designed a SGHS that concentrated on optimizing impedance matching in the upper half to facilitate greater microwave entry and on enhancing attenuation capability in the lower half to enable more efficient microwave absorption. Excellent MA performance was achieved through HFSS EM simulation.

## 2 Experiment

### 2.1 Materials

All chemical reagents used in this experiment were analytically pure without further purification processes. Ferric nitrate nonahydrate ( $\text{Fe}(\text{NO}_3)_3 \cdot 9\text{H}_2\text{O}$ , 98.5%) and 2,6-NDC (98%) were bought from Shanghai Macklin Biochemical Co., Ltd (Shanghai, China). N,N-Dimethylformamide (DMF, 99.5%) was bought from Modern Oriental (Beijing) Technology Development Co., Ltd (Beijing, China). Methanol was purchased from Shanghai Titan Scientific Co., Ltd (Shanghai, China). Nitrogen ( $\text{N}_2$ , high-purity) was purchased from Beijing Qianxi Jingcheng Gas Co., Ltd (Beijing, China). PVDF was obtained from Suzhou Sinero Technology Co., Ltd (Suzhou, China).

### 2.2 Synthesis of MIL-88C (Fe)

MIL-88C (Fe) was synthesized using an oil bath method, a modified version of a previously reported fabrication procedure [29]. Initially, 8 mL of DMF was stirred magnetically for 10 min with 75 mg (0.18 mmol)  $\text{Fe}(\text{NO}_3)_3 \cdot 9\text{H}_2\text{O}$  and 4 mg (0.018 mmol) 2,6-NDC (M/O = 10:1). Subsequently, the mixture was subjected to heating in an oil bath set at 110 °C for a duration of 10 min. The obtained products underwent a triple washing procedure after natural

cooling involving three cycles of rinsing with DMF and methanol, utilizing centrifugation ( $8000 \text{ r min}^{-1}$ , 2 min) for each step. Finally, the specimens were desiccated in a vacuum oven set at 60 °C for the entire night. The synthesized samples were designated as 88C-1 in Table 1. Simultaneously, the synthesis conditions for 88C-2, 88C-3, and 88C-4 are documented in Table 1. Notably, the quantity of the organic ligand remained constant.

### 2.3 Fabrication of Carbon Coating Iron-Based Composites

The MIL-88C (Fe) prepared above served as the precursor and was then pyrolyzed under nitrogen at 800 °C for 2 h with a temperature rise rate of  $5 \text{ }^\circ\text{C min}^{-1}$ . The obtained specimens derived from 88C-1, 88C-2, 88C-3, and 88C-4 were named as MD<sub>1</sub>, MD<sub>2</sub>, MD<sub>3</sub>, and MD<sub>4</sub>, respectively.

### 2.4 Preparation of MOF-Derivatives/PVDF Coaxial Rings

The total mass of MOF-derivatives (MD<sub>1</sub>, MD<sub>2</sub>, MD<sub>3</sub>, or MD<sub>4</sub>) and PVDF was 120 mg. The filling amounts of MOF-derivatives were 5 wt% (6 mg), 10 wt% (12 mg), 15 wt% (18 mg), and 20 wt% (24 mg), respectively. Initially, a certain number of MOF-derivatives and PVDF were dispersed by ultrasound in 5 mL of DMF for 30 min. Then, the homogeneous dispersion was transferred to an oven to evaporate at 90 °C for 4 h to obtain a flexible black film. The flexible black film was put into a special mold and pressed at 220 °C and 5 MPa for 15 min, then naturally cooled to room temperature to obtain the coaxial ring ( $\Phi_{\text{out}} = 7.00 \text{ mm}$  and  $\Phi_{\text{in}} = 3.04 \text{ mm}$ ).

**Table 1** Naming rules for materials

MOF	Conditions		
	M/O	Oil bath temperature (°C)	Oil bath time (min)
88C-1	10:1	110	10
88C-2	10:1	100	10
88C-3	2:1	110	10
88C-4	10:1	110	30

## 2.5 Material Characterization

The tests of crystal structure and phase composition of materials were conducted utilizing a Rigaku Smartlab SE X-ray diffraction (XRD) instrument employing Cu  $K\alpha$  radiation with a scanning rate of  $5^\circ \text{ min}^{-1}$ . The surface features and internal constitution of the specimens were investigated via scanning electron microscopy (SEM, ZEISS Sigma 300) and transmission electron microscopy (TEM, FEI TECNAI F20). The elemental composition and spatial distribution were characterized via energy-dispersive X-ray spectrometry (EDS, Ultim Max 100). Raman spectra were documented using a high-resolution confocal microscopy laser Raman instrument (WITec alpha300R) with a 532 nm laser source. The elemental electronic structure and valence state of the materials surface were revealed via X-ray photoelectron spectroscopy (XPS, Thermo Scientific K-Alpha) employing Al  $K\alpha$  radiation. The magnetic hysteresis loops were tested by vibrating sample magnetometer (VSM, Lake Shore 7404). Thermogravimetry (TG, Netzsch STA 449 F5 Jupiter) analysis was carried out under  $\text{N}_2$  atmosphere with a heating rate of  $10^\circ \text{ C min}^{-1}$ . Fourier transform infrared (FT-IR) spectra were acquired using an IRAffinity-1 spectrometer with spectral grade KBr sheets. The EM parameters of the coaxial rings were measured with a coaxial approach using a vector network analyzer (VNA Agilent TE5071C).

## 3 Results and Discussion

### 3.1 Characterizations of the As-Synthesized Materials

The preparation process of the derivatives from MIL-88C (Fe) and the absorbers mixed with PVDF is depicted in Scheme 1. The MIL-88C (Fe) has a three-dimensional (3D) hexagonal structure, in which trimeric units of  $\text{Fe}_3\text{O}$  are linked by  $\text{NDC}^{2-}$  to form a periodic 3D structure of  $[\text{Fe}_3\text{O}(\text{NDC})_3(\text{H}_2\text{O})_2(\text{NO}_3)]_n$  [29, 30]. Anisotropic growth leads to a hexagonal rod shape (Fig. 1a). Interestingly, the M/O, oil bath temperatures, and oil bath times were able to change AR. Specifically, increasing the M/O, lowering the oil bath temperature, or extending the oil bath time can raise the AR of MIL-88C (Fe). Iron ions ( $\text{Fe}^{3+}$ ) play a significant role in directional growth, and the larger their

amount, the longer the nanorods grow. The temperature of the oil bath affects the nucleation rate. The lower the temperature, the fewer the crystal nuclei, and accordingly, the longer the nanorods will be. The prolongation of reaction time leads to a more complete growth of the crystal along the axial direction. In addition, the sample surfaces became rough, and some small crystals were observed on their surfaces when the oil bath time was long enough. This phenomenon reveals that dissolution–recrystallization may occur on the material surfaces. The pyrolysis process consists of two stages: carbonization and graphitization. For pure organic materials, the graphitization process requires high temperatures above  $1000^\circ \text{ C}$ . If metal components are used as a catalyst, the temperature required for graphitization can be reduced to below  $1000^\circ \text{ C}$  [31]. Therefore, in this work, iron and metal compounds containing Fe, generated during pyrolysis, play catalytic roles in the graphitization process. After pyrolysis, the derivatives shrank in size due to the decomposition of organic ligands. And their surfaces became rough with a large number of nanoparticles of variable sizes evenly distributed on surfaces, but they still retained the basic shape of the precursors (Fig. 1b/1c). In the case of  $\text{MD}_3$ , for example, the results of EDS indicated the content of O was higher than it should be in  $\text{Fe}_3\text{O}_4$  (Fig. S1). It demonstrates that there are other forms of O present. Figure S2 illustrates the FT-IR results of  $\text{MD}_3$ , with peaks observed at  $1634$  and  $1400 \text{ cm}^{-1}$  corresponding to the symmetric and asymmetric stretching modes, respectively, of the carboxyl groups in 2,6-NDC [32]. Furthermore, the fact that the derivative retained the basic shape of the precursor also indicated that the organic ligand had not completely collapsed. Both of the above results suggest that the excess O is present in organic ligands.

TEM and HRTEM were used to further obtain the component and structural information of materials (Fig. 2). For  $\text{MD}_1$ ,  $\text{MD}_2$ ,  $\text{MD}_3$ , and  $\text{MD}_4$ , the TEM results all showed that the iron-based components were encapsulated in carbon. The iron-based phases of  $\text{MD}_1$  and  $\text{MD}_2$  exhibited small and dense structures (Fig. 2a<sub>1</sub>/b<sub>1</sub>), whereas  $\text{MD}_3$  and  $\text{MD}_4$  displayed bulky and sparse characteristics (Fig. 2c<sub>1</sub>/d<sub>1</sub>). The HRTEM results clearly revealed lattice stripes representing different components or various crystal faces of a specific component (Fig. 2a<sub>2</sub> ~ d<sub>2</sub>/a<sub>3</sub> ~ d<sub>3</sub>). The distinct lattice stripes of 0.48, 0.30, and 0.25 nm corresponded to the (111), (220), and (311) planes of  $\text{Fe}_3\text{O}_4$ , respectively

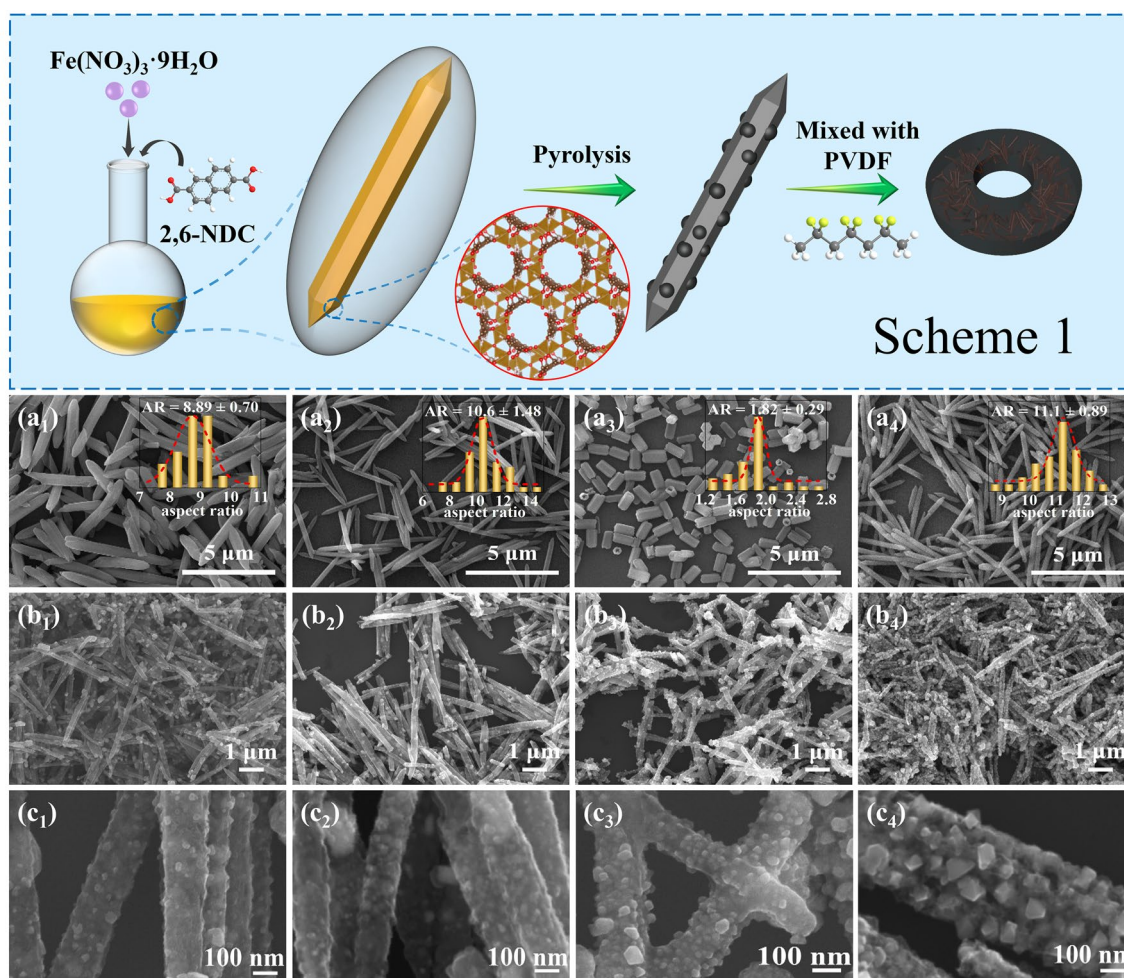


**Fig. 1** (Scheme 1) Forming process of carbon-coated iron-based composites and absorbers; SEM images and AR normal distribution of precursors: **a**<sub>1</sub> 88C-1, **a**<sub>2</sub> 88C-2, **a**<sub>3</sub> 88C-3, and **a**<sub>4</sub> 88C-4; Corresponding derivatives and their local enlargement: **b**<sub>1</sub>, **c**<sub>1</sub> MD<sub>1</sub>, **b**<sub>2</sub>, **c**<sub>2</sub> MD<sub>2</sub>, **b**<sub>3</sub>, **c**<sub>3</sub> MD<sub>3</sub>, and **b**<sub>4</sub>, **c**<sub>4</sub> MD<sub>4</sub>

(Fig. 2b<sub>3</sub>, c<sub>2-3</sub>, d<sub>2-3</sub>). The lattice fringes of 0.20 nm were attributed to the (110) plane of Fe (Fig. 2d<sub>3</sub>). The curved lattice fringes of 0.34 nm in Fig. 2a<sub>2</sub>~d<sub>2</sub> belonged to the (002) plane of graphitic carbon (GC), where the lattice fringes in Fig. 2a<sub>2</sub>/b<sub>2</sub> were more continuous and multilayered. The diffraction circles and spots observed in the selected area electron diffraction (SAED) patterns further demonstrated the existence of the corresponding phases (Fig. 2a<sub>4</sub>~d<sub>4</sub>), proving the polycrystalline structure. The elemental mapping results demonstrated the existence and even dispersion of Fe, O, and C elements (Fig. 2a<sub>5</sub>~d<sub>5</sub>).

The XRD result (Fig. S3) indicated the successful synthesis of precursor MIL-88C (Fe). As shown in Fig. 3a<sub>1</sub>, Fe-containing phases in the derivatives included Fe

(JCPDS: 06-0696), Fe<sub>3</sub>O<sub>4</sub> (JCPDS: 88-0315), or Fe<sub>3</sub>C (JCPDS: 34-0001). For the carbon component, MD<sub>1</sub> and MD<sub>2</sub> were dominated by GC (JCPDS: 34-0567) (Fig. 3a<sub>1</sub>). The broad peaks of MD<sub>3</sub> and MD<sub>4</sub> at about 20~30° represented the (002) plane of amorphous carbon (AC) (Fig. 3a<sub>2</sub>) [33]. The specific phases of the derivatives were as follows: MD<sub>1</sub> and MD<sub>4</sub> (Fe/Fe<sub>3</sub>O<sub>4</sub>/Fe<sub>3</sub>C@C), MD<sub>2</sub> (Fe/Fe<sub>3</sub>O<sub>4</sub>@C), and MD<sub>3</sub> (Fe<sub>3</sub>O<sub>4</sub>@C), in good agreement with HRTEM and SAED results. Notably, Fe phases are present in all the composites except MD<sub>3</sub>. This occurrence may be attributed to the high M/O conditions, where the O content of the organic ligand is not sufficient to react with all Fe<sup>3+</sup> ions to form Fe<sub>3</sub>O<sub>4</sub>. Consequently, the surplus Fe<sup>3+</sup> ions are reduced to Fe phases.

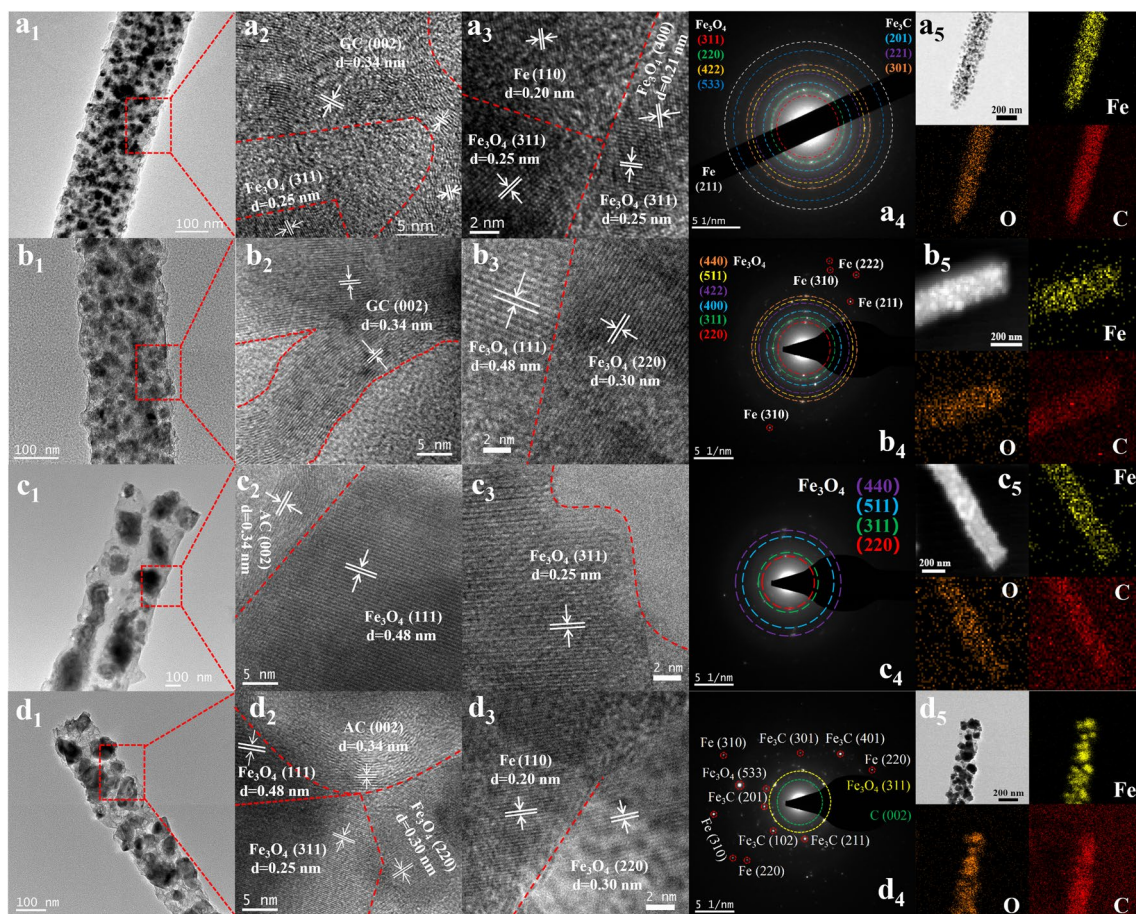


**Fig. 2** 1 TEM images, 2–3 HRTEM images, 4 SAED patterns, and 5 element mapping for Fe, O, and C of **a** MD<sub>1</sub>, **b** MD<sub>2</sub>, **c** MD<sub>3</sub>, and **d** MD<sub>4</sub>

Raman spectroscopy, an effective bulk characterization method, is used for analyzing the carbonaceous materials. The peaks at the 1350 and 1580 Raman shifts in Fig. 3b represent the D and G peaks of the carbonaceous materials. The D peak serves as an indicator of imperfections within the carbonaceous materials, here including  $sp^3$ -C in amorphous carbon and flaws in the  $sp^2$ -hybridized mesh. The G peak indicates perfect graphite consisting of  $sp^2$ -hybridized carbon [34, 35]. The  $I_D/I_G$  intensity ratio is frequently employed to depict both the level of graphitization and the presence of defects within carbon materials. Figure 3b shows the Raman spectra of the derivatives. The  $I_D/I_G$  results for MD<sub>1</sub>, MD<sub>2</sub>, MD<sub>3</sub>, and MD<sub>4</sub> were 0.81, 0.88, 1.03, and 2.82, respectively, indicating a decreasing order in the degree of graphitization. The aforementioned findings are also in alignment with the carbon diffraction peaks in the XRD results. The degree of graphitization was related to the type and size of the Fe-containing phases used as catalysts. Specially, the MD<sub>2</sub> had

iron-based components with the same small sizes as MD<sub>1</sub> but lacked the Fe<sub>3</sub>C phase, which made it have a slightly lower graphitization degree than MD<sub>1</sub>. For MD<sub>3</sub>, it only had Fe<sub>3</sub>O<sub>4</sub> with a larger size and therefore had an elevated value of  $I_D/I_G$  as well as a lower level of graphitization. Although MD<sub>4</sub> had the same iron-based components as MD<sub>1</sub>, the larger size of the iron-based phases left less room for the carbon component and therefore also had a lower degree of graphitization. Moreover, the broad 2D peaks near 2700  $\text{cm}^{-1}$  represent the presence of several layers of graphite, and the narrow 2D peaks represent multiple layers of graphite [36]. The conclusions drawn from the 2D peaks were in accordance with the HRTEM results. The above results indicate that the content of  $\text{Fe}^{3+}$ , the oil bath temperature, and the oil bath time affect the phases and degree of graphitization of the derivatives.

The XPS results are presented in Fig. 3c. The survey spectra (Fig. 3c<sub>1</sub>) showed that the composites contained C,

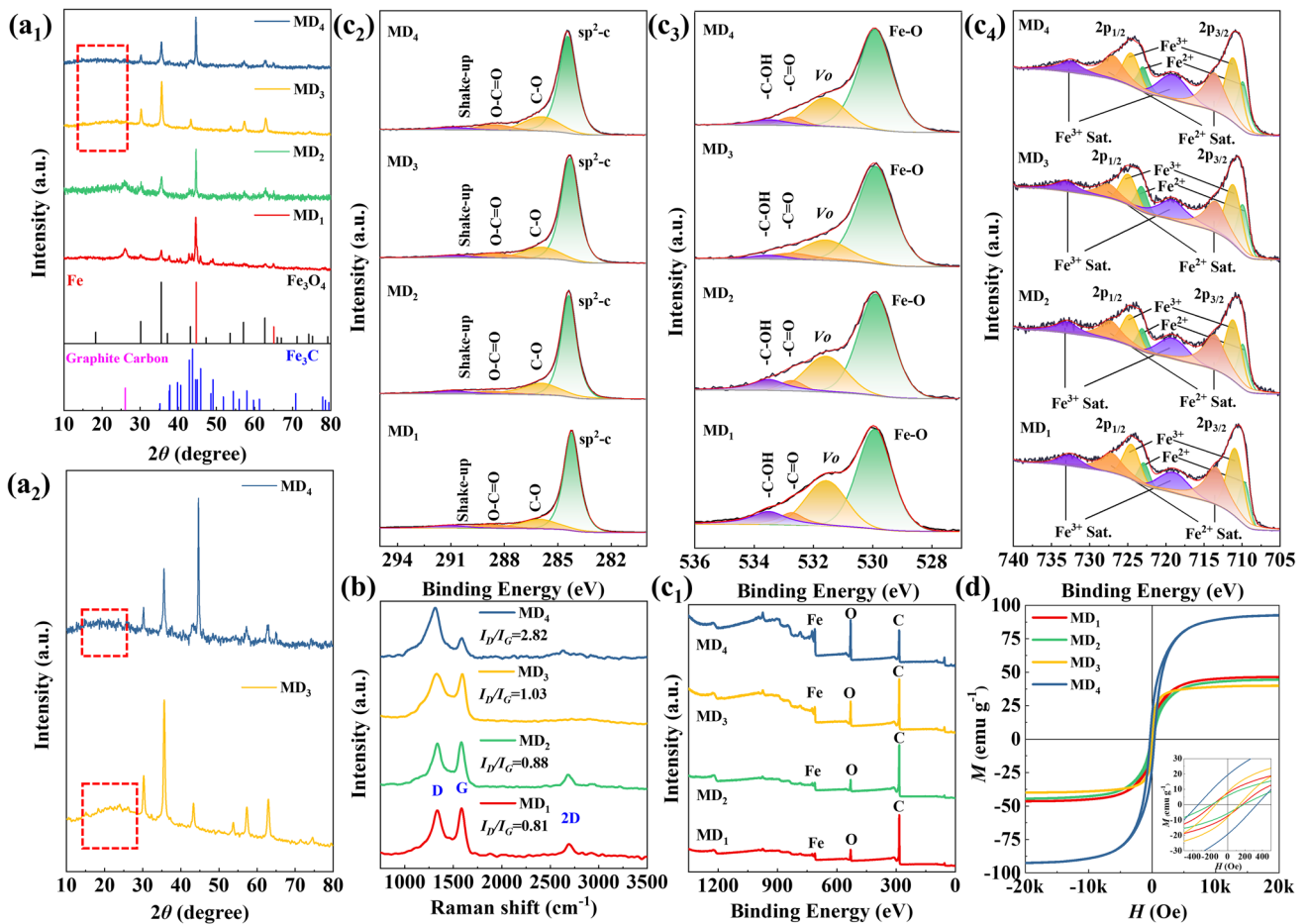


**Fig. 3** **a**<sub>1</sub> XRD images, **a**<sub>2</sub> XRD localized enlargement, **b** Raman spectra, XPS spectra: **c**<sub>1</sub> survey spectrum, **c**<sub>2</sub> C 1s, **c**<sub>3</sub> O 1s, and **c**<sub>4</sub> Fe 2p, and **d** hysteresis loops of MD<sub>1</sub>, MD<sub>2</sub>, MD<sub>3</sub>, and MD<sub>4</sub>

O, and Fe elements. The intensity of the C peaks indicated that MD<sub>1</sub> and MD<sub>2</sub> had higher and similar carbon content, whereas MD<sub>3</sub> and MD<sub>4</sub> exhibited sequentially lower carbon content. The peaks at 284.3 eV represented *sp*<sup>2</sup>-C, which demonstrated the material surface to be mainly graphite (Fig. 3c<sub>2</sub>). Meanwhile, the peaks representing carboxyl groups from the undecomposed organic ligand 2,6-DNC were also present. In the narrow spectra of the O element (Fig. 3c<sub>3</sub>), the two peaks with lower binding energies were attributed to the lattice oxygen (529.9 eV) and vacancy oxygen (*V*<sub>o</sub>) in Fe<sub>3</sub>O<sub>4</sub> (531.6 eV) [37]. The two remaining peaks at 532.7 eV and 533.5 eV denoted the oxygen in the carboxyl group, further demonstrating the existence of the undecomposed organic ligand 2,6-DNC. As shown in Fig. 3c<sub>4</sub>, the Fe element mainly consisted of two valence states of “+2” and “+3,” which indicated that the material surface was

mainly Fe<sub>3</sub>O<sub>4</sub>, while the Fe and Fe<sub>3</sub>C were mainly present in the bulk phases.

The magnetic properties of the composites are reflected by the saturation magnetization (*M*<sub>s</sub>) and coercivity (*H*<sub>c</sub>) from the VSM results (Fig. 3d). In particular, MD<sub>4</sub> presented a ferromagnetic hysteresis loop with the maximum *M*<sub>s</sub> of 92.5 emu g<sup>-1</sup> and *H*<sub>c</sub> of 331.6 Oe, which is due to the fact that it contains multifarious and bulky ferromagnetic components and low carbon content. MD<sub>3</sub> displayed the minimal *M*<sub>s</sub> of 39.9 emu g<sup>-1</sup> and *H*<sub>c</sub> of 131.5 Oe. This is attributed to the reason that it has only a single magnetic component Fe<sub>3</sub>O<sub>4</sub> and high carbon content. The values of *M*<sub>s</sub> and *H*<sub>c</sub> for MD<sub>1</sub> (46.4 emu g<sup>-1</sup>, 161.2 Oe) and MD<sub>2</sub> (44.5 emu g<sup>-1</sup>, 181.2 Oe) are almost equal. The *M*<sub>s</sub> of MD<sub>2</sub> is slightly lower than that of MD<sub>1</sub> due to the absence of Fe<sub>3</sub>C in MD<sub>2</sub> compared to MD<sub>1</sub>. Although MD<sub>1</sub> and MD<sub>4</sub> have the same variety of

ferromagnetic compositions, MD<sub>1</sub> has a higher carbon content than MD<sub>4</sub>. Therefore, the  $M_s$  and  $H_c$  of MD<sub>1</sub> are considerably lower than those of MD<sub>4</sub>.

To determine the suitable temperature for obtaining carbon-coated iron-based composites, the TG curve of 88C-3 under N<sub>2</sub> conditions was examined (Fig. S4). The mass loss was 4.4 wt% in stage I, corresponding to the loss of guest H<sub>2</sub>O molecules. The mass loss of 7.6 wt% in stage II was attributed to the removal of coordinated H<sub>2</sub>O and DMF molecules. With the increase in temperature, the large mass loss of 26.7 wt% in stage III corresponded to the decomposition of organic ligands. The mass loss of 12.7 wt% in the last stage IV indicated complete decomposition of organic ligands [38], culminating at ~800 °C with a total weight loss of 51.4 wt%. Consequently, derivatives with adequate pyrolysis can be obtained at 800 °C.

### 3.2 MA Performance of Absorbers Derived From MIL.88C (Fe)

The values of  $RL$  and EAB are major indicators to assess the MA properties.  $RL$  values can be counted using the subsequent two equations [39]:

$$RL = 20 \log \left| \frac{Z_{in} - Z_0}{Z_{in} + Z_0} \right| \quad (1)$$

$$Z_{in} = Z_0 \sqrt{\frac{\mu_r}{\epsilon_r}} \tanh \left[ j \left( \frac{2f\pi d}{c} \right) \sqrt{\mu_r \epsilon_r} \right] \quad (2)$$

where the normalized input impedance of the absorbers and free space is represented by  $Z_{in}$  and  $Z_0$ , respectively.  $\epsilon_r$  and  $\mu_r$  denote the relative complex permittivity ( $\epsilon_r = \epsilon' - j\epsilon''$ ) and complex permeability ( $\mu_r = \mu' - j\mu''$ ).  $f$  represents the incident EM wave frequency,  $d$  denotes the thickness of the absorbers, and  $c$  signifies the speed of light propagation in vacuum.  $RL < -10$  dB means the absorber possesses MA properties, and EAB designates the frequency region wherein  $RL < -10$  dB. To fully exploit the MA performance of the absorbers, we chose PVDF instead of wax as the matrix. The effect of PVDF and wax as substrates on the MA properties was compared using MD<sub>3</sub> as an example (Fig. S5). As shown in Fig. S5a<sub>1/2</sub>, the  $\epsilon'$  and  $\epsilon''$  of MD<sub>3</sub>/PVDF are significantly higher than those of MD<sub>3</sub>/wax for the same filling amount (10 wt%), consistent with previous studies [40]. The notable increase in the dielectric constant is attributed to dipole polarization resulting from the difference in electronegativity between F/H atoms and C atoms, as well as interfacial polarization

occurring between PVDF and MD<sub>3</sub> [41, 42]. The value of  $\mu'$  and  $\mu''$  has not changed significantly (Fig. S5b<sub>1/2</sub>). Therefore, choosing PVDF as the substrate can significantly enhance the MA properties (Fig. S5c<sub>1/2</sub>). Additionally, PVDF can be utilized to construct flexible MAM characterized by corrosion resistance and excellent mechanical properties. It also demonstrates process feasibility and practicality in engineering applications compared to wax substrates.

As shown in Fig. 4a<sub>1</sub> and S6a<sub>1</sub>, MD<sub>1</sub>/PVDF (5 wt%) had a minimum  $RL$  of -30.0 dB at 17.6 GHz (1.4 mm) and the EAB was 4.8 GHz (1.61 mm). As the filling amount increased, the MA properties became progressively worse (Fig. 4a<sub>2/3</sub> and Fig. S6a<sub>2/4</sub>). In comparison, the optimal  $RL$  of MD<sub>2</sub>/PVDF (5 wt%) rose to -55.6 dB at 16.64 GHz (1.72 mm), and the EAB broadened to 5.52 GHz (1.90 mm) (Fig. 4b<sub>1</sub> and Fig. S6b<sub>1</sub>). Compared to MD<sub>1</sub>/PVDF at the same filling amounts, MD<sub>3</sub>/PVDF and MD<sub>4</sub>/PVDF achieved a leap from none to excellent MA properties. In Fig. 4b<sub>2</sub> and Fig. S6c<sub>2</sub>, the  $RL_{min}$  of MD<sub>3</sub>/PVDF (10 wt%) was -67.4 dB at 12.56 GHz (2.13 mm), and the EAB was 4.96 GHz (1.78 mm). In Fig. 4b<sub>3</sub> and Fig. S6d<sub>4</sub>, the  $RL_{min}$  of MD<sub>4</sub>/PVDF (20 wt%) was -59.3 dB at 10.4 GHz (2.17 mm), and the EAB was 4.88 GHz (1.56 mm). The filler loadings of absorbers have a significant effect on the MA performance. The MA properties of MD<sub>1</sub>/PVDF, MD<sub>2</sub>/PVDF, MD<sub>3</sub>/PVDF, and MD<sub>4</sub>/PVDF at various filler loadings are displayed in Fig. S6 and Fig. S7.

Notably, the graphitization degree and AR together influence the optimum filler loading, with the degree of graphitization being the main factor. The greater the level of graphitization, the more readily a conductive network. MD<sub>1</sub> had the highest degree of graphitization and a large AR, resulting in an optimal filler amount as low as 5 wt%. MD<sub>2</sub> was slightly less graphitized than MD<sub>1</sub> but had a larger AR than MD<sub>1</sub>, so the optimum filler loading could also be as low as 5 wt%. Compared to MD<sub>1</sub>, MD<sub>3</sub> had a low degree of graphitization and a small AR; thus, it had an optimal filler amount of 10 wt%. Although MD<sub>4</sub> had the largest AR, the degree of graphitization was the lowest, therefore the optimum filler loading was 20 wt%.

Generally speaking, two essential factors dictate the MA properties. The primary consideration is impedance matching coefficient ( $M_z$ ). For samples with finite thickness, utilizing  $M_z$  to evaluate impedance matching characteristics is more reasonable [43], and value near 1.0 indicates a well-matched impedance, with a large number of EM waves able to be introduced into materials.

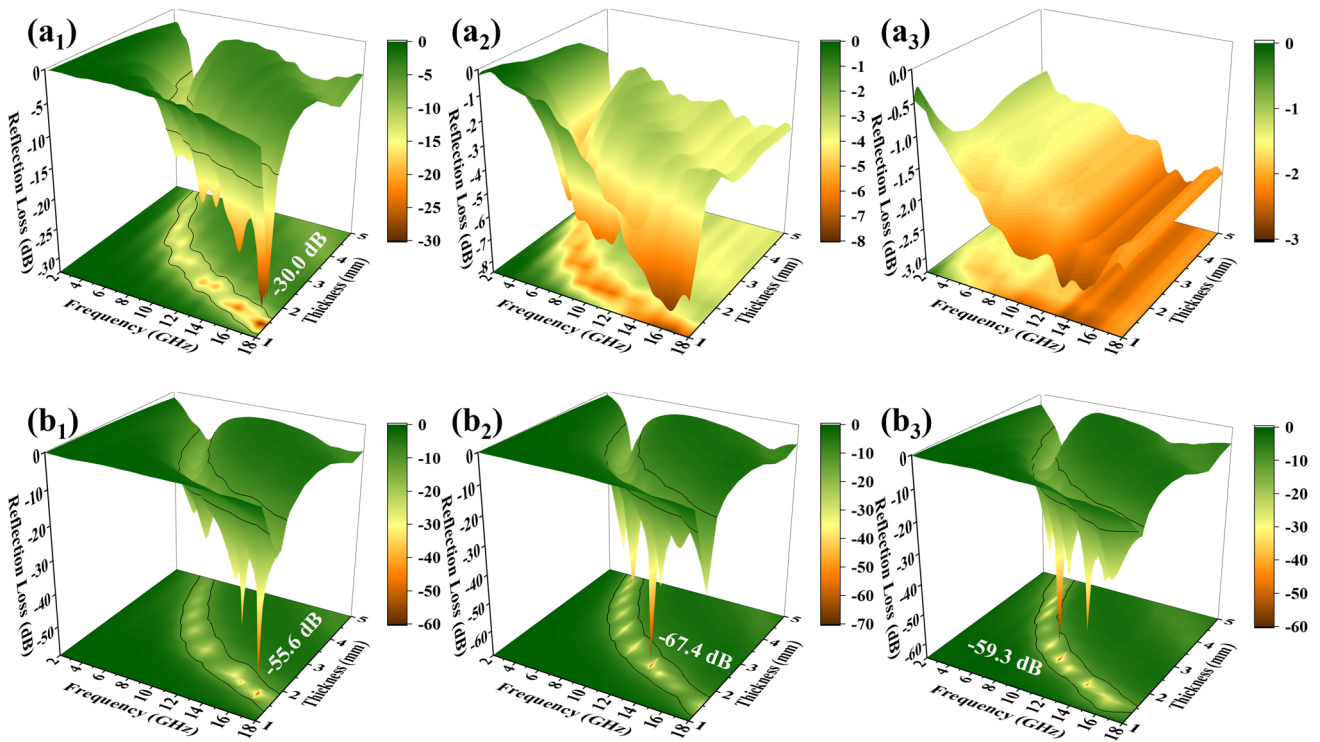


**Fig. 4** 3D RL curves of MD<sub>1</sub>/PVDF at filler loading of **a**<sub>1</sub> 5 wt%, **a**<sub>2</sub> 10 wt%, and **a**<sub>3</sub> 20 wt%; **b**<sub>1</sub> MD<sub>2</sub>/PVDF at filler loading of 5 wt%, **b**<sub>2</sub> MD<sub>3</sub>/PVDF at filler loading of 10 wt%, and **b**<sub>3</sub> MD<sub>4</sub>/PVDF at filler loading of 20 wt%

An assessment of the impedance matching capability of absorbers is conducted within the range of 0.8 to 1.0 [34]. Besides good impedance matching, MA performance is also influenced by the attenuation constant ( $\alpha$ ). The value of  $M_z$  and  $\alpha$  were determined by the subsequent equations [34, 44]:

$$M_z = \frac{2Z'_{in}}{|Z'_{in}|^2 + 1} \tag{3}$$

$$\alpha = \frac{\sqrt{2\pi f}}{c} \sqrt{(\mu''\epsilon'' - \mu'\epsilon') + \sqrt{(\mu''\epsilon'' - \mu'\epsilon')^2 + (\mu'\epsilon'' + \mu''\epsilon')^2}} \tag{4}$$

where the  $Z'_{in}$  is the real input impedance, where the parameters  $\epsilon'$ ,  $\mu'$ ,  $\epsilon''$ , and  $\mu''$  are real and imaginary parts of relative complex permittivity and permeability, respectively. As shown in Fig. 5a<sub>1</sub>/b<sub>1</sub>, MD<sub>2</sub>/PVDF (5 wt%) possessed a greater impedance matching area delineated with the white dotted lines and more  $Z$  values close to 1 than MD<sub>1</sub>/PVDF (5 wt%). The values of  $\alpha$  for both are close to each other, indicating similar attenuation capacities (Fig. 5c<sub>1</sub>). As a result, MD<sub>2</sub>/PVDF (5 wt%) had a stronger RL and a wider EAB. In

Fig. 5a<sub>2</sub>/a<sub>3</sub>, MD<sub>1</sub>/PVDF (10 wt%) and MD<sub>1</sub>/PVDF (20 wt%) had poor impedance matching. This is due to the high graphitization degree, which makes MD<sub>1</sub>/PVDF easier to form conductive networks, resulting in higher dielectric constants within high filler loadings (Fig. S8). Notably, for MD<sub>1</sub>/PVDF within a filler loading of 20 wt%, the  $\epsilon''$  is greater than  $\epsilon'$ , which indicates the formation of a conductive network resembling a conductor at high filler levels, leading to skin effects [45]. Due to the impedance mismatch, even though MD<sub>1</sub>/PVDF (10 wt%) and MD<sub>1</sub>/PVDF (20 wt%) had higher loss capacities (Fig. 5c<sub>2</sub>/c<sub>3</sub>), they could not exhibit MA properties. In contrast, both MD<sub>3</sub>/PVDF (10 wt%) and MD<sub>4</sub>/PVDF (20 wt%) had excellent impedance matching (Fig. 5b<sub>2</sub>/b<sub>3</sub>), combined with suitable dissipation capacities, and therefore exhibited excellent MA performance.

EM parameters were analyzed in depth for the purpose of further exploring the MA mechanism of the three excellent absorbers. The real parts ( $\epsilon'$  and  $\mu'$ ) signify the storage capability of electrical and magnetic energy, while the imaginary parts ( $\epsilon''$  and  $\mu''$ ) indicate the ability to dissipate EM energy. The  $\epsilon'$  values in Fig. S9a<sub>1</sub> exhibit an overall downward trend from 13 to 7, 8, or 10 approximately with

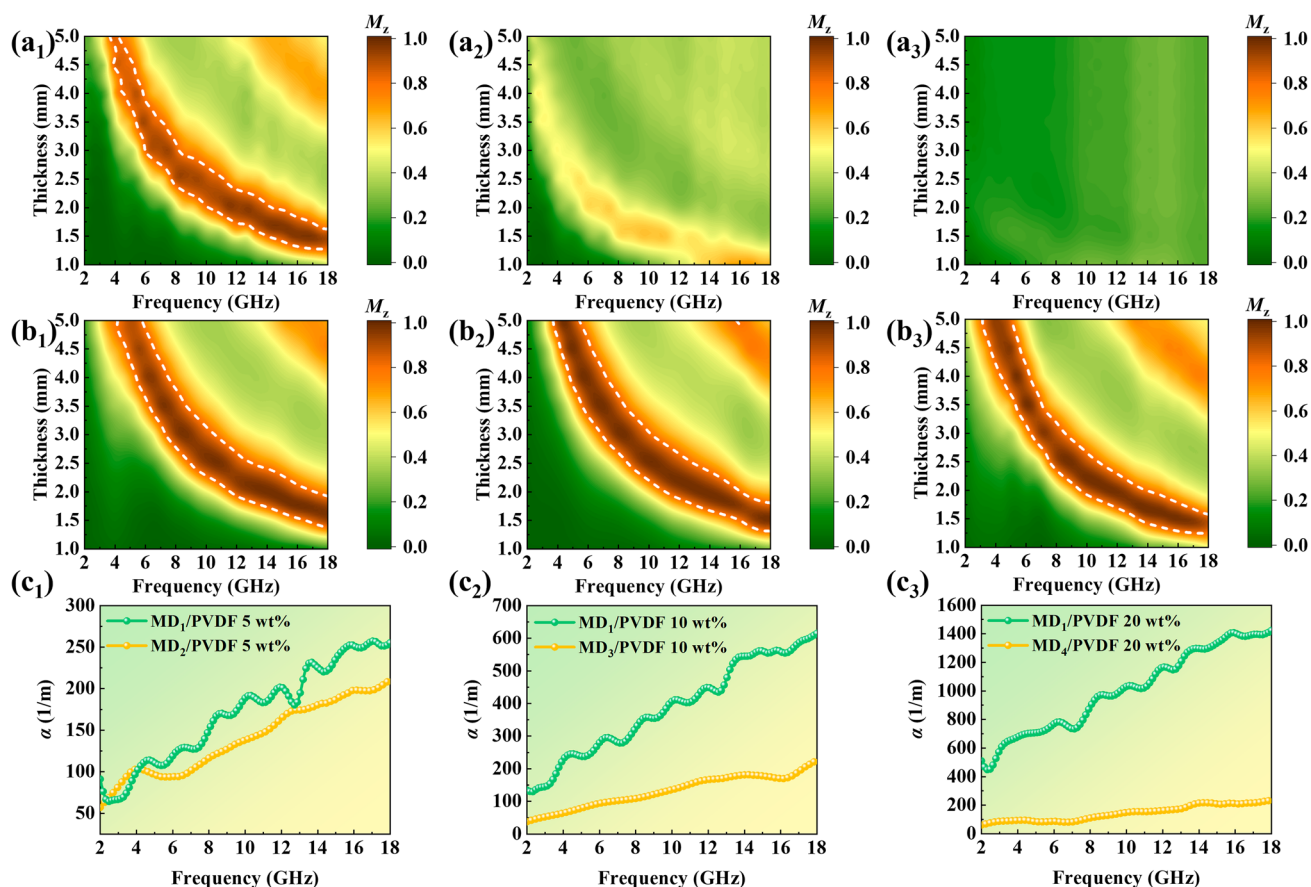


**Fig. 5** 2D contour map of the  $M_z$  value of MD<sub>1</sub>/PVDF at filler loading of **a**<sub>1</sub> 5 wt%, **a**<sub>2</sub> 10 wt%, and **a**<sub>3</sub> 20 wt%; **b**<sub>1</sub> MD<sub>2</sub>/PVDF at filler loading of 5 wt%, **b**<sub>2</sub> MD<sub>3</sub>/PVDF at filler loading of 10 wt%, and **b**<sub>3</sub> MD<sub>4</sub>/PVDF at filler loading of 20 wt%; **c**<sub>1</sub>~**c**<sub>3</sub> Contrast values for attenuation constants  $\alpha$

increasing frequency, exhibiting the dispersion effect. The  $\epsilon''$ - $f$  graphs of the three absorbers were observed in Fig. S9a<sub>2</sub>, and the curves all exhibited an overall decreasing trend from 7.6 to 3.6, 5.2 to 3.3, and 5.7 to 2.9, respectively. This represents the conductivity loss and small resonance peaks represent the polarization loss [46]. The MD<sub>4</sub>/PVDF had the highest number of resonant peaks, the MD<sub>2</sub>/PVDF the second most, and the MD<sub>3</sub>/PVDF the least. The dielectric loss tangent ( $\tan\delta_\epsilon = \epsilon''/\epsilon'$ ) was computed to assess the ability of absorbers to lose electrical energy, and the corresponding curves showed the same trend as  $\epsilon''$  (Fig. S9a<sub>3</sub>). Figure S9b<sub>1/2</sub> display the  $\mu'$ - $f$  and  $\mu''$ - $f$  graphs of the three absorbers, and the presence of resonance peaks is observed, indicating that the absorbers have magnetic loss capability to some extent. Some negative  $\mu''$  values of the MD<sub>2</sub>/PVDF may result from the induced alternating magnetic field generated by the motion

of free electrons within the alternating electric field, leading to the radiation of magnetic energy from the conductive networks [47]. The values of the magnetic loss tangent ( $\tan\delta_\mu = \mu''/\mu'$ ) are also computed to assess the ability to lose magnetic energy (Fig. S9b<sub>3</sub>). By comparison, the value of  $\tan\delta_\epsilon$  is higher than  $\tan\delta_\mu$ , demonstrating that the contribution of dielectric loss to the MA performance of absorbers predominates over magnetic loss.

Types of microwave loss can be classified from both component and micro/macroscopic geometric structure perspectives. The component level includes dielectric loss caused by dielectric materials and magnetic loss from magnetic materials. Dielectric loss comprises conduction loss and polarization relaxation within the range of 2~18 GHz. The Debye relaxation theory elucidates the mechanism underlying dielectric loss, and it can be summarized the correlation for  $\epsilon'$  and  $\epsilon''$  as [48]:

$$\left(\epsilon' - \frac{\epsilon_s + \epsilon_\infty}{2}\right)^2 + (\epsilon'')^2 = \left(\frac{\epsilon_s + \epsilon_\infty}{2}\right)^2 \tag{5}$$

where  $\epsilon_s$  stands for the static dielectric constant as the frequency approaches 0, while  $\epsilon_\infty$  denotes the permittivity in the limit as frequency approaches infinity. The  $\epsilon'$ - $\epsilon''$  curve of the three absorbers exhibited a shape accompanied by several Cole–Cole semicircles in the high frequency range and a straight line in the low frequency range in Fig. S9c<sub>1-3</sub>. This indicates that the dielectric loss included the contributions of polarization and conduction losses. The semicircles depict the process of relaxation polarization, encompassing dipole polarization, defect-induced polarization, and interface polarization. The dipole polarization was caused by the variance in electronegativity between F/H atoms and C atoms in PVDF and dangling bonds on the surface of Fe<sub>3</sub>O<sub>4</sub> [49]. The defect-induced polarization was generated by carbon defects [50], grain boundaries [51], and Vo in Fe<sub>3</sub>O<sub>4</sub> [52]. The interface polarization was formed by various heterogeneous interfaces with different electronegativity, including GC, AC [53], PVDF, and iron-based components. The MD<sub>4</sub>/PVDF had the largest number of semicircles due to the most iron components (Fe, Fe<sub>3</sub>O<sub>4</sub>, and Fe<sub>3</sub>C), and these iron components produced more interfacial polarization. Additionally, the number of semicircles observed was in accordance with the regularity of resonance peak occurrences in the  $\epsilon''$ - $f$  curves. The straight lines demonstrate the conductive loss attributed to GC. Generally, the magnetic loss within the 2~18 GHz range includes eddy current loss, natural resonance, and exchange resonance. The analysis of magnetic loss type involves the calculation of the value of  $C_0$  using the following equation [54]:

$$C_0 = \mu''(\mu')^{-2}f^{-1} \tag{6}$$

In Fig. S10, the three absorbers all exhibited a clear fluctuation trend between 2~8 GHz and a constant trend within the band of 8~18 GHz. This phenomenon proves that the magnetic loss was caused by natural resonance (2~8 GHz) and eddy current loss (8~18 GHz). As MD<sub>2</sub>/PVDF and MD<sub>4</sub>/PVDF contained more magnetic components, both fluctuated more significantly between 2~8 GHz, indicating more significant magnetic resonance losses occurred.

Besides the component perspective, the types of microwave loss in terms of micro/macrosopic geometric structure, including dissipation of the reflected EM wave and multiple scattering, also play a key role. The dissipation of the reflected EM wave can be analyzed based on  $\lambda/4$  theory via the subsequent equation [55]:

$$t_m = \frac{n\lambda}{4} = \frac{nc}{4f_m \sqrt{|\epsilon_r||\mu_r|}} (n = 1, 3, 5 \dots) \tag{7}$$

where  $t_m$  represents the matching thickness, and  $f_m$  represents for the frequency corresponding to the optimal  $RL$  value under the matching thickness.  $\lambda$  and  $c$  are the corresponding microwave lengths and the velocity of light in vacuo.  $|\epsilon_r|$  and  $|\mu_r|$  denote the moduli of the relative complex permittivity and permeability. The  $\lambda/4$  model leads to a different phase of  $\pi$  between reflection waves from the front and back of absorbers, which results in a reflection wave extinction effect and promotes MA performance [55]. The coordinate points corresponding to the actual situation of the three absorbers were compliant to the  $f_m - t_m$  curve within the error range (Fig. S11) [43]. It demonstrates that optimum  $RL$  versus matching thickness is in accordance with a specific rule and the optimal  $RL$  values are obtained at the most matched thicknesses. Meanwhile, the  $M_z$  values at optimum thicknesses are extremely close to 1.0. Furthermore, randomly distributed nanorods tend to scatter EM waves multiple times, extending the propagation path and facilitating the conversion of EM energy into heat.

### 3.3 MA Mechanisms of Derivatives From MIL.88C (Fe)

The potential mechanisms of MA for the absorbers are illustrated in Fig. 6. The combination of moderate dielectric constants and certain permeabilities facilitated optimal impedance matching and obtained suitable attenuation constants. The random distribution of graphite-containing derivatives constituted a 3D conductive network that promoted electron migration and hopping, thereby exhibiting conductive loss properties. Defects such as carbon defects, vacancies, and grain boundaries in the composites induced and trapped electrons, resulting in polarization induced by defects. Dipole polarizations were generated by inherent dipoles in PVDF and dangling bonds on Fe<sub>3</sub>O<sub>4</sub> surfaces. More interfacial polarizations were also created among multiple phases. The magnetic components Fe, Fe<sub>3</sub>O<sub>4</sub>, and Fe<sub>3</sub>C converted EM energy into thermal energy through magnetic resonance and eddy currents. All the mechanisms discussed above were examined at the component level. Furthermore, micro/macrosopic geometric structural aspects such as multiple scattering and  $\lambda/4$  theory were also significant in MA.

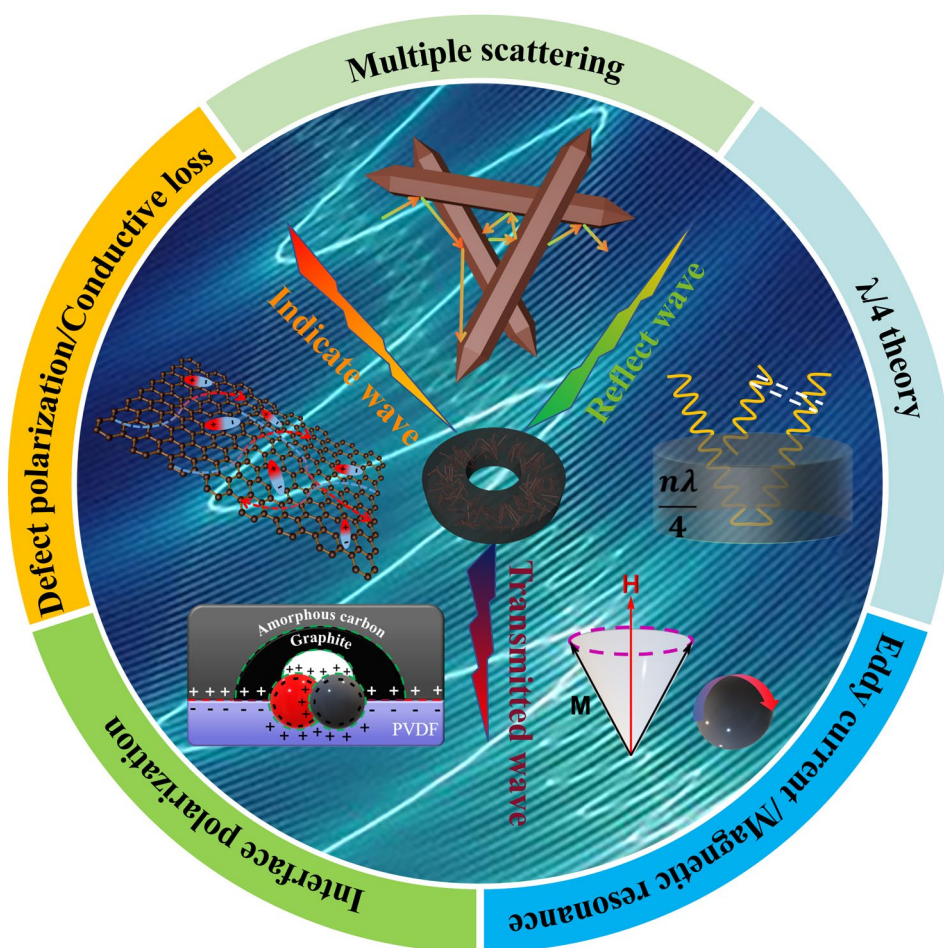


**Fig. 6** Schematic illustration of MA mechanisms for the derivatives of MIL-88C (Fe)

### 3.4 Comparison of MA Performance

Eventually, a specific reflection loss (SRL) value is introduced to properly assess the MA capability considering both filler loading and thickness. It can be calculated as follows [56]:

$$\text{SRL} = \frac{\text{RL}}{\text{Filling loading} \times \text{Thickness}} \quad (8)$$

We compared the SRL values of the MD<sub>2</sub>/PVDF and MD<sub>3</sub>/PVDF with those of recent advanced absorbers, as shown in Fig. 7. The specific performance data of the above absorbers are listed in Table S1. Surprisingly, our work exhibited minimal SRL values compared to other absorbers, indicating stronger reflection loss, thinner thickness, and lower filler loading.

### 3.5 EM Simulation Results of the SGHS

To further investigate the absorption results of the SGHS, simulations were conducted using HFSS in accordance with the finite element method and transmission line theory. As shown in Fig. 8a, the SGHS model was created with the pink border representing an air box, the bottom blue plate serving as an aluminum plate, and the SGHS in the middle section. Two sets of master–slave boundaries were established (Fig. 8b, c), with the Freud excitation boundary acting as the incident direction and the scanning port serving as the corresponding detection direction (Fig. 8d). During the EM simulation, a periodic structure was assembled through repetition of the honeycomb model. Simultaneously, the EM parameters of MD<sub>3</sub>/PVDF (10 wt%) were imported into the software. EM waves were incident vertically from directly

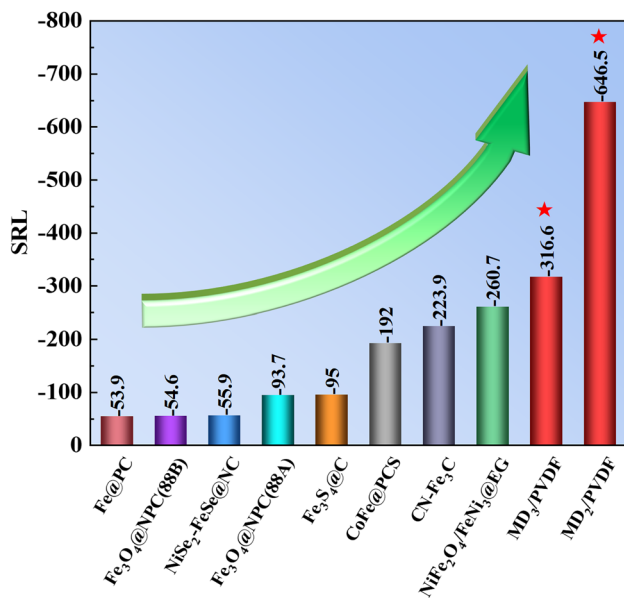


**Fig. 7** Comparison of SRL of MD<sub>2</sub>/PVDF and MD<sub>3</sub>/PVDF with the current advanced absorbers

above the honeycomb model. The parameters of the SGHS model are presented in Fig. 8e, including the hexagonal honeycomb side length ( $R$ ) at the top and bottom of the model, the hexagonal honeycomb side length ( $r$ ) in the middle of the model, and the thickness ( $H$ ).

The MA performance of SGHS is determined by its structural features. Therefore, this study focused on investigating the impact of the parameters ( $H$ ,  $r$ , and  $R$ ) on the MA properties of the SGHS. Thickness ( $H$ ) has vital importance in honeycomb structures and significantly influences MA properties [57, 58]. As illustrated in Fig. S12a, both the  $RL$  and EAB of the SGHS increased notably with an increase in thickness. The minimum  $RL_{\min}$  of -59.0 dB was achieved when  $H = 30$  mm,  $r = 7.5$  mm, and  $R = 9$  mm. Figure S12b depicts the impact of  $r$  on the MA performance of the SGHS.  $RL$  strengthened as  $r$  decreased within a certain range, but continued reduction in  $r$  led to  $RL$  weakening. This is attributed to the decrease in  $r$  causing an increase in the gradient of the honeycomb holes, which, to some extent, promotes impedance matching, enabling greater penetration of EM waves from the upper half [59, 60]. Simultaneously, the significant gradient of the symmetric lower half facilitates better multiple scattering of EM waves, resulting in excellent MA performance. However, excessively small  $r$  hinders the entry of EM waves into the SGHS. Meanwhile, EAB increased with decreasing  $r$ , continuously expanding

the effective absorption of the SGHS at low frequencies. Notably, when  $r$  (8.5 mm) and  $R$  (9 mm) are nearly equal, the structure resembles the conventional through-hole honeycomb structure, exhibiting poorer MA performance. This indicates a significant advantage of the SGHS over the conventional honeycomb structure. The impact of  $R$  on the MA performance of the SGHS aligned with that of  $r$  (Fig. S12c). The maximum EAB of 14.6 GHz (3.4~18.0 GHz) occurred at parameters  $H = 30$  mm,  $r = 7.5$  mm, and  $R = 13$  mm. The gradient of the honeycomb hole is fixed when the difference between  $R$  and  $r$  is certain. Under the condition of fixed honeycomb hole gradients, the  $RL$  curves of the structures had the same trend when  $R$  and  $r$  were varied simultaneously (Fig. S12d). This demonstrates the substantial impact of the honeycomb hole gradient on the MA properties of the SGHS. In summary, the parameters of the SGHS can be chosen based on the particular demands for MA performance.

To further analyze the MA mechanism of the SGHS, Fig. 8 presents the distribution of electric field and vector, magnetic field and vector, volume loss density, and Poynting vector at 10 GHz. In Fig. 8f<sub>1</sub>, in the upper half of the SGHS, the electric field strength increases closer to the honeycomb hole, suggesting that a significant quantity of microwaves penetrates the honeycomb hole. The decreasing gradient of the electric field in the lower half of the SGHS indicates a gradual attenuation of microwaves during transmission. Figure 8f<sub>2</sub> shows that the local current mainly travels along the wall of the SGHS ( $y$ -direction), concentrating primarily above and below the cross section where the honeycomb holes are situated. The geometric properties of the SGHS wall enable a longer path for local current conduction, which is advantageous [57]. The magnetic field distribution was approximated to the electric field distribution, and the results similarly indicated that massive microwaves entered through the honeycomb holes in the upper half of the SGHS and were absorbed in the lower half (Fig. 8g<sub>1</sub>). The direction of the magnetic moments mainly aligned with the honeycomb wall ( $x$ -direction, perpendicular to the direction of the local current), and likewise, they predominantly concentrated near the cross section where the honeycomb holes were positioned (Fig. 8g<sub>2</sub>). The results of the volume loss density distribution highlighted that the loss occurs throughout the SGHS (Fig. 8h). The Poynting vector, being an energy flow density vector in the EM field, visualized the distribution of EM energy in the SGHS (Fig. 8i). The results effectively validate the initial design conjecture. The gradient structure

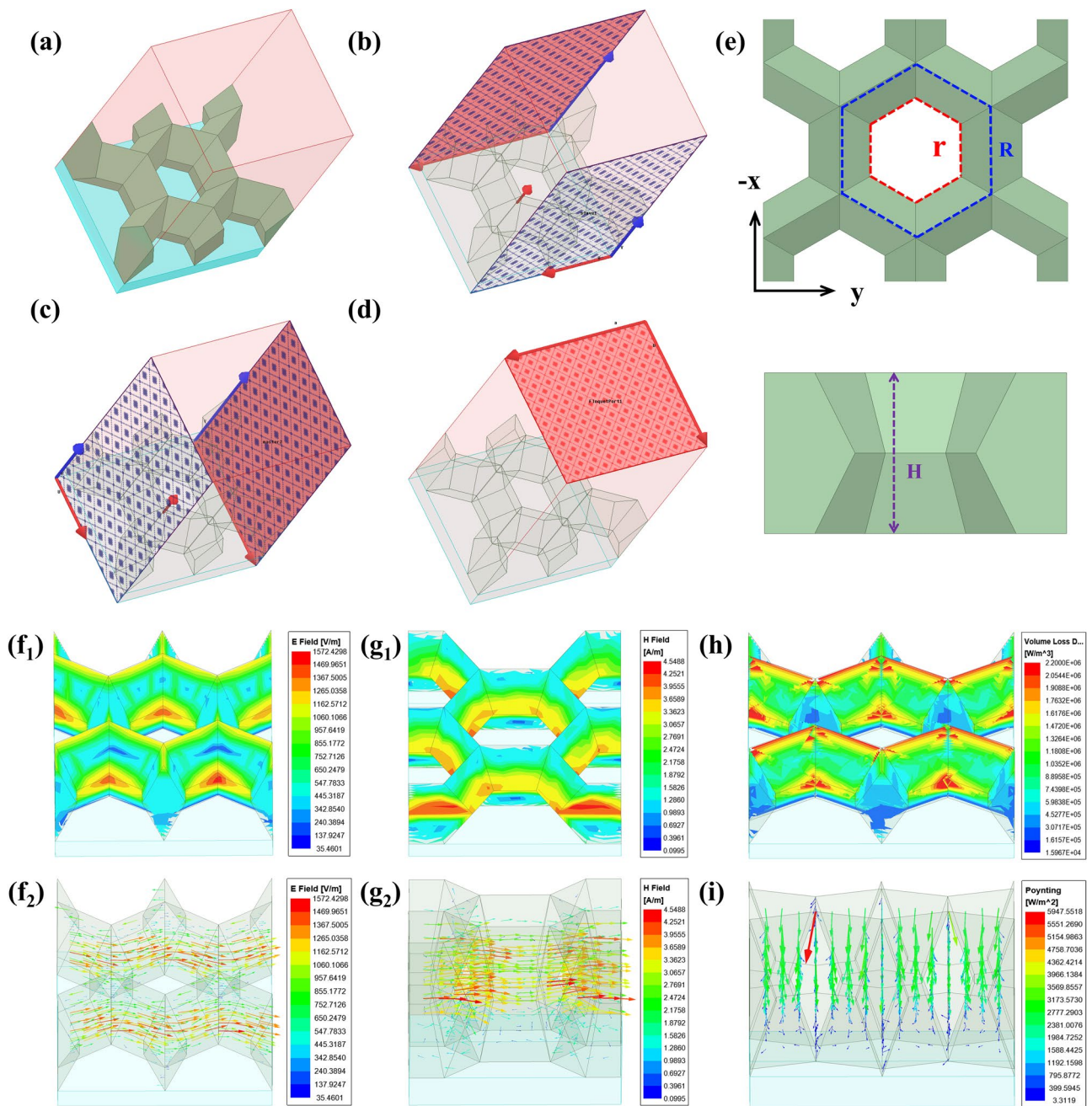


**Fig. 8** **a** SGHS model; **b**, **c** two sets of master–slave boundaries; **d** sources of excitation for the model; **e** parameters related to the SGHS; **f**<sub>1</sub> Simulated electric field and **f**<sub>2</sub> electric field vector distribution of the SGHS at 10 GHz; **g**<sub>1</sub> Simulated magnetic field and **g**<sub>2</sub> magnetic field vector distribution of the SGHS at 10 GHz; **h** Volume loss density distribution of the SGHS at 10 GHz; **i** Poynting vector distribution of the SGHS at 10 GHz

of the upper half contributes to the optimization of impedance matching, thereby allowing more microwaves to enter. The symmetric gradient structure of the lower half is better able to confine microwaves, promoting multiple reflection

and scattering of the microwaves, extending the transmission path, and depleting EM energy.

## 4 Conclusion

In summary, we systematically synthesized a range of MIL-88C (Fe) precursors with varying AR under diverse preparation conditions, subsequently acquiring the corresponding carbon-coated iron-based derivatives using identical pyrolysis conditions. It is concluded that alterations in the preparation conditions of the MIL-88C (Fe) precursor impact the phases, graphitization degree, and AR of the derivatives, influencing the optimum filling amount, impedance matching, and MA properties. The MD<sub>2</sub>/PVDF, MD<sub>3</sub>/PVDF, and MD<sub>4</sub>/PVDF absorbers demonstrated outstanding MA properties with optimal filler loadings below 20 wt%, some as low as 5 wt%. The MD<sub>2</sub>/PVDF (5 wt%) achieved a maximum EAB of 5.52 GHz (1.90 mm). The MD<sub>3</sub>/PVDF (10 wt%) exhibited a  $RL_{\min}$  value of -67.4 dB at 12.56 GHz (2.13 mm). Additionally, the absorbers prepared in this study displayed minimal SRL values compared to most existing absorbers, signifying stronger RL, thinner thickness, and lower filler content. Through HFSS EM simulation, the integration of the material benefits of MD<sub>3</sub>/PVDF (10 wt%) with the structural advantages of the SGHS resulted in an EAB of 14.6 GHz and a  $RL_{\min}$  of -59.0 dB. It is well suited for the demands of real engineering applications and will prove to be promising candidates in the MA field.

**Acknowledgements** This project was financially supported by the National Natural Science Foundation of China (51972049, 52073010, and 52373259), the Projects of the Science and Technology Department of Jilin Province (20230201132GX), and the Projects of the Education Department of Jilin Province (JJKH20220123KJ). The authors would like to thank Shiyanjia Lab ([www.shiyanjia.com](http://www.shiyanjia.com)) for the XRD, Raman, XPS, and VSM characterizations.

### Declarations

**Conflict of interest** The authors declare that they have no known competing financial interests or personal relationships that could have appeared to influence the work reported in this paper.

**Open Access** This article is licensed under a Creative Commons Attribution 4.0 International License, which permits use, sharing, adaptation, distribution and reproduction in any medium or format, as long as you give appropriate credit to the original author(s) and the source, provide a link to the Creative Commons licence, and indicate if changes were made. The images or other third party material in this article are included in the article's Creative Commons licence, unless indicated otherwise in a credit line to the material. If material is not included in the article's Creative Commons licence and your intended use is not permitted by statutory

regulation or exceeds the permitted use, you will need to obtain permission directly from the copyright holder. To view a copy of this licence, visit <http://creativecommons.org/licenses/by/4.0/>.

**Supplementary Information** The online version contains supplementary material available at <https://doi.org/10.1007/s40820-024-01435-z>.

## References

1. Y. Zhang, L. Zhang, L. Tang, R. Du, B. Zhang, S-NiSe/HG nanocomposites with balanced dielectric loss encapsulated in room-temperature self-healing polyurethane for microwave absorption and corrosion protection. *ACS Nano*. **18**, 8411–8422 (2024). <https://doi.org/10.1021/acsnano.3c13057>
2. Z. Wu, X. Tan, J. Wang, Y. Xing, P. Huang et al., MXene hollow spheres supported by a C-Co exoskeleton grow MWCNTs for efficient microwave absorption. *Nano-Micro Lett.* **16**, 107 (2024). <https://doi.org/10.1007/s40820-024-01326-3>
3. X. Yan, X. Huang, B. Zhong, T. Wu, H. Wang et al., Balancing interface polarization strategy for enhancing electromagnetic wave absorption of carbon materials. *Chem. Eng. J.* **391**, 123538 (2020). <https://doi.org/10.1016/j.cej.2019.123538>
4. L. Liu, H. Deng, X. Tang, Y. Lu, J. Zhou et al., Specific electromagnetic radiation in the wireless signal range increases wakefulness in mice. *Proc. Natl. Acad. Sci. U.S.A.* **118**, e2105838118 (2021). <https://doi.org/10.1073/pnas.2105838118>
5. K. Zhang, Y. Liu, Y. Liu, Y. Yan, G. Ma et al., Tracking regulatory mechanism of trace Fe on graphene electromagnetic wave absorption. *Nano-Micro Lett.* **16**, 66 (2024). <https://doi.org/10.1007/s40820-023-01280-6>
6. H. Ma, M. Fashandi, Z.B. Rejeb, P. Gong, C.B. Park et al., Efficient electromagnetic wave absorption and thermal infrared stealth in PVTMS@MWCNT nano-aerogel via abundant nano-sized cavities and attenuation interfaces. *Nano-Micro Lett.* **16**, 20 (2024). <https://doi.org/10.1007/s40820-023-01218-y>
7. Z. Zhang, Z. Cai, Z. Wang, Y. Peng, L. Xia et al., A review on metal–organic framework-derived porous carbon-based novel microwave absorption materials. *Nano-Micro Lett.* **13**, 56 (2021). <https://doi.org/10.1007/s40820-020-00582-3>
8. L.T. Nguyen, C.J. Goh, T. Bai, R.H. Ong, X.Y. Goh et al., Scalable fabrication of lightweight carbon nanotube aerogel composites for full X-band electromagnetic wave absorption. *Carbon* **219**, 118811 (2024). <https://doi.org/10.1016/j.carbon.2024.118811>
9. Y. Xu, X. Huang, Y. Chen, Y. Liu, X. Long et al., A theoretical strategy of pure carbon materials for lightweight and excellent absorption performance. *Carbon* **174**, 662–672 (2021). <https://doi.org/10.1016/j.carbon.2020.11.044>
10. S.H. Kim, S.Y. Lee, Y. Zhang, S.J. Park, J. Gu, Carbon-based radar absorbing materials toward stealth technologies. *Adv.*



- Sci. **10**, 2303104 (2023). <https://doi.org/10.1002/advs.202303104>
11. Y. Du, Z. Yan, W. You, Q. Men, G. Chen et al., Balancing MXene surface termination and interlayer spacing enables superior microwave absorption. *Adv. Funct. Mater.* **33**, 2301449 (2023). <https://doi.org/10.1002/adfm.202301449>
  12. Y. Yan, K. Zhang, G. Qin, T. Zhang, X. Huang, Phase engineering on MoS<sub>2</sub> to realize dielectric gene engineering for enhancing microwave absorbing performance. *Adv. Funct. Mater.* (2023). <https://doi.org/10.1002/adfm.202316338>
  13. D. Pan, G. Yang, H.M. Abo-Dief, V. Murugadoss, N. Naik et al., Vertically aligned silicon carbide nanowires/boron nitride cellulose aerogel networks enhanced thermal conductivity and electromagnetic absorbing of epoxy composites. *Nano-Micro Lett.* **14**, 118 (2022). <https://doi.org/10.1007/s40820-022-00863-z>
  14. R. Hu, L. Li, X. Xu, D. Pan, J. Dong et al., Dimensional design of Fe<sub>0.9</sub>Co<sub>0.1</sub> nano-alloys with enhanced low-frequency microwave absorption. *Chem. Eng. J.* **482**, 148864 (2024). <https://doi.org/10.1016/j.cej.2024.148864>
  15. M. Yu, S. Li, X. Ren, N. Liu, W. Guo et al., Magnetic bimetallic heterointerface nanomissiles with enhanced microwave absorption for microwave thermal/dynamics therapy of breast cancer. *ACS Nano* **18**, 3636–3650 (2024). <https://doi.org/10.1021/acsnano.3c11433>
  16. R.C. Che, L.M. Peng, X.F. Duan, Q. Chen, X.L. Liang, Microwave absorption enhancement and complex permittivity and permeability of Fe encapsulated within carbon nanotubes. *Adv. Mater.* **16**, 401–405 (2004). <https://doi.org/10.1002/adma.200306460>
  17. J.R. Choi, E. Cho, H. Lee, S.B. Lee, W.R. Yu et al., Synthesis of Fe/Co bimetallic metal-organic framework-derived composites and their enhanced electromagnetic wave absorption. *Adv Compos Hybrid Mater* **7**, 26 (2024). <https://doi.org/10.1007/s42114-023-00824-z>
  18. S. Surblé, C. Serre, C. Mellot-Draznieks, F. Millange, G. Férey, A new isorecticular class of metal-organic-frameworks with the MIL-88 topology. *Chem. Commun.* **3**, 284–286 (2006). <https://doi.org/10.1039/B512169H>
  19. C. Serre, C. Mellot-Draznieks, S. Surblé, N. Audebrand, G. Férey et al., Role of solvent-host interactions that lead to very large swelling of hybrid frameworks. *Science* **315**, 1828–1831 (2007). <https://doi.org/10.1126/science.1137975>
  20. Y. Dong, X. Zhu, F. Pan, B. Deng, Z. Liu, Mace-like carbon fiber/ZnO nanorod composite derived from *Typha orientalis* for lightweight and high-efficient electromagnetic wave absorber. *Adv. Compos. Hybrid Mater.* **4**, 1002–1014 (2021). <https://doi.org/10.1007/s42114-021-00277-2>
  21. J. Shi, Q. Zhuang, L. Wu, R. Guo, L. Huang et al., Molecular engineering guided dielectric resonance tuning in derived carbon materials. *J. Mater. Chem. C* **10**, 12257–12265 (2022). <https://doi.org/10.1039/D2TC02628G>
  22. N. Wu, D. Xu, Z. Wang, F. Wang, J. Liu et al., Achieving superior electromagnetic wave absorbers through the novel metal-organic frameworks derived magnetic porous carbon nanorods. *Carbon* **145**, 433–444 (2019). <https://doi.org/10.1016/j.carbon.2019.01.028>
  23. Z. Xiang, Y. Song, J. Xiong, Z. Pan, X. Wang et al., Enhanced electromagnetic wave absorption of nanoporous Fe<sub>3</sub>O<sub>4</sub> @ carbon composites derived from metal-organic frameworks. *Carbon* **142**, 20–31 (2019). <https://doi.org/10.1016/j.carbon.2018.10.014>
  24. Z.X. Liu, H.B. Yang, Z.M. Han, W.B. Sun, X.X. Ge et al., A bioinspired gradient design strategy for cellulose-based electromagnetic wave absorbing structural materials. *Nano Lett.* **24**, 881–889 (2024). <https://doi.org/10.1021/acs.nanolett.3c03989>
  25. Z. Zhang, H. Lei, S. Duan, Z. Zhao, M. Chen et al., Bioinspired double-broadband switchable microwave absorbing grid structures with inflatable kresling origami actuators. *Adv. Sci.* **11**, 2306119 (2024). <https://doi.org/10.1002/advs.202306119>
  26. D.D. Lim, S. Lee, J.H. Lee, W. Choi, G.X. Gu, Mechanical metamaterials as broadband electromagnetic wave absorbers: investigating relationships between geometrical parameters and electromagnetic response. *Mater. Horiz.* (2024). <https://doi.org/10.1039/D3MH01959D>
  27. H. Yan, S. Xuan, X. Fan, Y. Shan, X. Xu et al., A repair efficiency evaluation framework for the honeycomb microwave absorbing structure. *Compos. Sci. Technol.* **248**, 110471 (2024). <https://doi.org/10.1016/j.compscitech.2024.110471>
  28. C. Wang, S. Ma, D. Li, J. Zhao, H. Zhou et al., Direct ink writing of thermoresistant, lightweight composite polyimide honeycombs with tunable X-band electromagnetic wave absorption properties. *Addit. Manuf.* **70**, 103554 (2023). <https://doi.org/10.1016/j.addma.2023.103554>
  29. G. Lee, S. Lee, S. Oh, D. Kim, M. Oh, Tip-to-middle anisotropic MOF-on-MOF growth with a structural adjustment. *J. Am. Chem. Soc.* **142**, 3042–3049 (2020). <https://doi.org/10.1021/jacs.9b12193>
  30. C. Serre, F. Millange, S. Surblé, G. Férey, A route to the synthesis of trivalent transition-metal porous carboxylates with trimeric secondary building units. *Angew. Chem. Int. Ed.* **116**, 6445–6449 (2004). <https://doi.org/10.1002/ange.200454250>
  31. Y. Ding, Z.A. Qiao, Carbon surface chemistry: new insight into the old story. *Adv. Mater.* **34**, 2206025 (2022). <https://doi.org/10.1002/adma.202206025>
  32. Y. Zhang, C.M. Liang, M. Lu, H. Yu, G.S. Wang, Skillful introduction of urea during the synthesis of MOF-derived FeCoNi-CH/p-rGO with a spindle-shaped substrate for hybrid supercapacitors. *ACS Omega* **7**, 33019–33030 (2022). <https://doi.org/10.1021/acsomega.2c02712>
  33. Y. Tang, J. Ding, W. Zhou, S. Cao, F. Yang et al., Design of uniform hollow carbon nanoarchitectures: different capacitive deionization between the hollow shell thickness and cavity size. *Adv. Sci.* **10**, 2206960 (2023). <https://doi.org/10.1002/advs.202206960>
  34. P.Y. Zhao, H.Y. Wang, B. Cai, X.B. Sun, Z.L. Hou et al., Electrospinning fabrication and ultra-wideband electromagnetic wave absorption properties of CeO<sub>2</sub>/N-doped carbon

- nanofibers. *Nano Res.* **15**, 7788–7796 (2022). <https://doi.org/10.1007/s12274-022-4675-x>
35. B. Sayahpour, H. Hirsh, S. Bai, N. Schorr, T. Lambert et al., Revisiting discharge mechanism of  $\text{CF}_x$  as a high energy density cathode material for lithium primary battery. *Adv. Energy Mater.* **12**, 2103196 (2022). <https://doi.org/10.1002/aenm.202103196>
36. H. Xu, X. Yin, X. Fan, Z. Tang, Z. Hou et al., Constructing a tunable heterogeneous interface in bimetallic metal-organic frameworks derived porous carbon for excellent microwave absorption performance. *Carbon* **148**, 421–429 (2019). <https://doi.org/10.1016/j.carbon.2019.03.091>
37. Q. Chang, H. Liang, B. Shi, H. Wu, Microstructure induced dielectric loss in lightweight  $\text{Fe}_3\text{O}_4$  foam for electromagnetic wave absorption. *iScience* **25**, 103925 (2022). <https://doi.org/10.1016/j.isci.2022.103925>
38. N. Tsumori, L. Chen, Q. Wang, M. Kitta, Q. Xu et al., Quasi-MOF: exposing inorganic nodes to guest metal nanoparticles for drastically enhanced catalytic activity. *Chem* **4**, 845–856 (2018). <https://doi.org/10.1016/j.chempr.2018.03.009>
39. H.Y. Wang, X.B. Sun, Y. Xin, S.H. Yang, P.F. Hu et al., Ultrathin self-assembly MXene/Co-based bimetallic oxide heterostructures as superior and modulated microwave absorber. *J. Mater. Sci. Technol.* **134**, 132–141 (2023). <https://doi.org/10.1016/j.jmst.2022.05.061>
40. X.J. Zhang, G.S. Wang, Y.Z. Wei, L. Guo, M.S. Cao, Polymer-composite with high dielectric constant and enhanced absorption properties based on graphene-CuS nanocomposites and polyvinylidene fluoride. *J. Mater. Chem. A* **1**, 12115–12122 (2013). <https://doi.org/10.1039/C3TA12451G>
41. H.Y. Wang, X.B. Sun, S.H. Yang, P.Y. Zhao, X.J. Zhang et al., 3D ultralight hollow NiCo compound@MXene composites for tunable and high-efficient microwave absorption. *Nano-Micro Lett.* **13**, 206 (2021). <https://doi.org/10.1007/s40820-021-00727-y>
42. S. Gao, G.S. Wang, L. Guo, S.H. Yu, Tunable and ultraefficient microwave absorption properties of trace N-doped two-dimensional carbon-based nanocomposites loaded with multi-rare earth oxides. *Small* **16**, 1906668 (2020). <https://doi.org/10.1002/sml.201906668>
43. Z.L. Hou, X. Gao, J. Zhang, G. Wang, A perspective on impedance matching and resonance absorption mechanism for electromagnetic wave absorbing. *Carbon* **222**, 118935 (2024). <https://doi.org/10.1016/j.carbon.2024.118935>
44. M. Tang, J.Y. Zhang, S. Bi, Z.L. Hou, X.H. Shao et al., Ultrathin topological insulator absorber: unique dielectric behavior of  $\text{Bi}_2\text{Te}_3$  nanosheets based on conducting surface states. *ACS Appl. Mater. Interfaces* **11**, 33285–33291 (2019). <https://doi.org/10.1021/acsami.9b13775>
45. X. Zhou, J. Wen, Z. Wang, X. Ma, H. Wu, Broadband high-performance microwave absorption of the single-layer  $\text{Ti}_3\text{C}_2\text{T}_x$  MXene. *J. Mater. Sci. Technol.* **115**, 148–155 (2022). <https://doi.org/10.1016/j.jmst.2021.11.029>
46. X. Zhou, B. Wang, Z. Jia, X. Zhang, X. Liu et al., Dielectric behavior of  $\text{Fe}_3\text{N}@C$  composites with green synthesis and their remarkable electromagnetic wave absorption performance. *J. Colloid Interface Sci.* **582**, 515–525 (2021). <https://doi.org/10.1016/j.jcis.2020.08.087>
47. L. Deng, M. Han, Microwave absorbing performances of multiwalled carbon nanotube composites with negative permeability. *Appl. Phys. Lett.* **91**, 023119 (2007). <https://doi.org/10.1063/1.2755875>
48. H.Y. Wang, X.B. Sun, G.S. Wang et al., A MXene-modulated 3D crosslinking network of hierarchical flower-like MOF derivatives towards ultra-efficient microwave absorption properties. *J. Mater. Chem. A* **9**, 24571–24581 (2021). <https://doi.org/10.1039/D1TA06505J>
49. G. Wu, Y. Cheng, Z. Yang, Z. Jia, H. Wu et al., Design of carbon sphere/magnetic quantum dots with tunable phase compositions and boost dielectric loss behavior. *Chem. Eng. J.* **333**, 519–528 (2018). <https://doi.org/10.1016/j.cej.2017.09.174>
50. Z. Tang, L. Xu, C. Xie, L. Guo, L. Zhang et al., Synthesis of  $\text{CuCo}_2\text{S}_4$ @expanded graphite with crystal/amorphous heterointerface and defects for electromagnetic wave absorption. *Nat. Commun.* **14**, 5951 (2023). <https://doi.org/10.1038/s41467-023-41697-6>
51. M. Qin, L. Zhang, H. Wu, Dielectric loss mechanism in electromagnetic wave absorbing materials. *Adv. Sci.* **9**, 2105553 (2022). <https://doi.org/10.1002/advs.202105553>
52. Y. Liu, X. Zhou, Z. Jia, H. Wu, G. Wu, Oxygen vacancy-induced dielectric polarization prevails in the electromagnetic wave-absorbing mechanism for Mn-based MOFs-derived composites. *Adv. Funct. Mater.* **32**, 2204499 (2022). <https://doi.org/10.1002/adfm.202204499>
53. Y. Liu, X. Wei, X. He, J. Yao, R. Tan et al., Multifunctional shape memory composites for Joule heating, self-healing, and highly efficient microwave absorption. *Adv. Funct. Mater.* **33**, 2211352 (2022). <https://doi.org/10.1002/adfm.202211352>
54. X.J. Zhang, J.Q. Zhu, P.G. Yin, A.P. Guo, A.P. Huang et al., Tunable high-performance microwave absorption of  $\text{Co}_{1-x}\text{S}$  hollow spheres constructed by nanosheets within ultralow filler loading. *Adv. Funct. Mater.* **28**, 1800761 (2018). <https://doi.org/10.1002/adfm.201800761>
55. M. Green, Z. Liu, P. Xiang, X. Tan, F. Huang et al., Ferric metal-organic framework for microwave absorption. *Mater. Today Chem.* **9**, 140–148 (2018). <https://doi.org/10.1016/j.mtchem.2018.06.003>
56. N. Yang, Z.X. Luo, G.R. Zhu, S.C. Chen, X.L. Wang et al., Ultralight three-dimensional hierarchical cobalt nanocrystals/N-doped CNTs/carbon sponge composites with hollow skeleton toward superior microwave absorption. *ACS Appl. Mater. Interfaces* **11**, 35987–35998 (2019). <https://doi.org/10.1021/acsami.9b11101>
57. H. Pang, Y. Duan, X. Dai, L. Huang, X. Yang et al., The electromagnetic response of composition-regulated honeycomb structural materials used for broadband microwave absorption. *J. Mater. Sci. Technol.* **88**, 203–214 (2021). <https://doi.org/10.1016/j.jmst.2021.01.072>
58. N. Zhang, M. Han, G. Wang, Y. Zhao, W. Gu et al., Achieving broad absorption bandwidth of the Co/carbon absorbers



- through the high-frequency structure simulator electromagnetic simulation. *J. Alloy. Compd.* **883**, 160918 (2021). <https://doi.org/10.1016/j.jallcom.2021.160918>
59. H. Yan, B. Fu, S. Xuan, T. Qin, X. Yao, Electromagnetic response of grading honeycomb composites for broadband microwave absorption. *Compos. Struct.* **321**, 117280 (2023). <https://doi.org/10.1016/j.compstruct.2023.117280>
60. F. Luo, D. Liu, T. Cao, H. Cheng, J. Kuang et al., Study on broadband microwave absorbing performance of gradient porous structure. *Adv. Compos. Hybrid Mater.* **4**, 591–601 (2021). <https://doi.org/10.1007/s42114-021-00275-4>